Geophysical Journal International

Geophys. J. Int. (2012) **189,** 513–523 doi: 10.1111/j.1365-246X.2011.05348.x

Differential *t** measurements via instantaneous frequency matching: observations of lower mantle shear attenuation heterogeneity beneath western Central America

Sean R. Ford[1] Edward J. Garnero[2] and Michael S. Thorne[3]

[1] *Ground-based Nuclear Detonation Detection Programs, Lawrence Livermore National Laboratory, Livermore, CA* 94550*, USA. E-mail: sean@llnl.gov*
[2] *School of Earth & Space Exploration, Arizona State University, Tempe, AZ* 85287*, USA*
[3] *Department of Geology & Geophysics, University of Utah, Salt Lake City, UT* 84112*, USA*

Accepted 2011 December 16. Received 2011 December 16; in original form 2011 August 23

SUMMARY

We infer shear attenuation in the lower mantle by using the method of instantaneous frequency matching to calculate differential t^* between core-reflected *ScS* and direct *S* (δt^*_{ScS-S}). The instantaneous frequency at the envelope peak of a seismic phase is related to the average Fourier spectral frequency of that phase. To estimate δt^*_{ScS-S} for a given trace, we first calculate the instantaneous frequency at the envelope peak of *S* and *ScS*. The trace is then attenuated through convolution with a suite of t^* operators until the instantaneous frequency at the envelope peak of the seismic phase with the initially larger instantaneous frequency matches the value of the smaller instantaneous frequency from the initial calculation. The differential t^* operator required to accomplish the match is then δt^*_{ScS-S}. We also calculate δt^*_{ScS-S} from the slope of the spectral ratio of windowed *ScS* and *S*. Both the spectral ratio and instantaneous frequency methods produce consistent results for high signal-to-noise ratio synthetic waveforms with *S* and *ScS* well separated in time, and where there are no other interfering phases. The instantaneous frequency method gives more stable results for low signal-to-noise ratio waveforms, and where *S* and/or *ScS* are affected by other interfering seismic phases. The instantaneous frequency matching method is applied to broadband data from South American earthquakes recorded in California that sample the lower mantle beneath Central America and the Cocos plate. δt^*_{ScS-S} ranges from approximately –4 to 2 s, but are predominately negative, suggesting *S* is more attenuated than *ScS* for these data. We estimate the possibly contaminating effects of 3-D velocity heterogeneity on δt^*_{ScS-S} through analysis of synthetic seismograms computed for a cross-section through a tomographically derived model of global shear wave heterogeneity, using an axisymmetric finite difference algorithm. Synthetics for path geometries of our data predict a δt^*_{ScS-S} of ∼0.2 s. We investigate the effect of seismic anisotropy by comparing δt^*_{ScS-S} before and after a subset of the data were corrected using splitting parameters obtained by linearizing the particle motion of the *S* and *ScS* phases. The rms error of the residuals between the corrected and uncorrected δt^*_{ScS-S} is ∼0.2 s. Neither of these efforts, however, match the large negative observed δt^*_{ScS-S} values, suggesting the mid-mantle beneath western Central America is in fact much more attenuating than the lowermost mantle below it, or *S* may be broadened by out-of-plane propagation effects, involving the remains of the Farallon plate containing stronger velocity heterogeneity than is imaged by seismic tomography.

Key words: Time-series analysis; Body waves; Seismic attenuation; Dynamics of lithosphere and mantle.

1 INTRODUCTION

There has been significant progress in determining the 3-D elastic shear structure of the lower mantle on global (e.g. Kuo *et al.* 2000; Mégnin & Romanowicz 2000; Grand 2002) and regional (e.g. Garnero 2000; Ni & Helmberger 2001; Wysession *et al.* 2001; Thomas *et al.* 2002) scales. And since the pioneering work of Anderson & Archambeau (1964), a first-order agreement on the

radial profile of attenuation, which is inversely proportional to the seismic quality factor Q [as defined by Knopoff (1964)], has emerged for the lower mantle based on free oscillation data (Anderson & Hart 1978; Dziewonski & Anderson 1981; Widmer *et al.* 1991; Durek & Ekstrom 1996 and for an insightful statistical analysis of several radial Q models see Resovsky *et al.* 2005). A different approach by Lawrence & Wysession (2006) that employs body waves found higher shear Q (Q_μ) in the lower mantle than previous studies. Lateral variations in mantle Q structure are routinely documented from analyses of long-period surface waves and free oscillations (Romanowicz 1995; Selby & Woodhouse 2002; Dalton & Ekstrom 2006), but possible lateral variations in lower mantle anelastic structure have not been well determined because of the decrease in resolution with increasing depth in the lower mantle for these long-period data. Thus, to estimate lateral Q variations at regional scales (100–1000 km) in the deepest mantle, relatively short wavelength body waves that sample the deep mantle must be used. However, the interpretation of Q studies is difficult because of the challenges of separating intrinsic Q from effective Q caused by focusing/defocusing and scattering of the wavefield because of propagation in 3-D heterogeneous elastic structure (Cormier 1982; Romanowicz 1998).

The dispersive effects of anelastic structure on velocity can be better modelled if Q is known (Futterman 1962). Karato (1993) showed that the density derivative of velocity is strongly affected by anelasticity, and concluded that Q_μ structure is very important when interpreting shear velocity models. Laboratory and theoretical studies have shown that Q_μ is more sensitive to temperature than velocity measurements (Minster & Anderson 1981; Karato & Spetzler 1990; Jackson 2000). Thus, determination of lateral variations in deep mantle Q may have important consequences, as models depicting a partial melt origin to reduced D$''$ (lowermost mantle layer just above the core boundary) shear wave speeds are not uncommon (e.g. Lay *et al.* 2004). And comparison of attenuation measurements with velocity, which is sensitive to compositional variations, should ultimately help to constrain the thermal versus chemical nature of seismically derived elastic heterogeneities, giving greater insight to dynamical processes in the mantle (Romanowicz & Durek 2000).

Attenuation of body waves has been investigated with both time-domain waveform modelling and in the frequency domain through spectral analysis (see discussion in Romanowicz & Mitchell (2007) and references therein). Theoretically, both approaches should yield similar results for Q. However, time-domain methods are susceptible to bias from noise and difficulties in synchronizing waveforms in time (Tonn 1989). Whereas, frequency-domain methods can suffer when the choice of bandwidth over which to make a spectral measurement either includes noise or doesn't contain the full spectral content of the signal, and also when a seismic phase of differing dominant period arrives closely in time to the phase of interest (Bhattacharyya 1998).

Here, we present the instantaneous frequency matching method (Matheney & Nowack 1995; Engelhard 1996; Dasios *et al.* 2001; Gao *et al.* 2011) for S and ScS, which can be considered a hybrid time-frequency approach to infer lower mantle lateral attenuation. We compare this differential attenuation measurement approach to the frequency-domain method of spectral ratios using synthetic waveforms, and find that it performs better in the presence of noise and interfering seismic phases. Using the instantaneous frequency matching method, we then measure differential attenuation between S and ScS on waveforms that traverse the lower mantle beneath western Central America, and explore the effects of anisotropy and elastic heterogeneity on the results.

2 METHODS

2.1 Spectral ratios

Differential attenuation between two phases can be calculated from the logarithmic of their spectral amplitude ratio (Kanamori 1967; Teng 1968; Bath 1974). The amplitude spectrum $A(\omega, \theta, \Delta)$ of a seismic phase can be given by

$$A(\omega, \theta, \Delta) = S(\omega)B(\theta, \Delta)R(\omega)I(\omega)G(\Delta)e^{-\omega t^*/2}, \tag{1}$$

where ω is the radial frequency, $S(\omega)$ is the source spectrum, $B(\theta, \Delta)$ is the source radiation pattern where θ is the exiting angle from the source and Δ is the source-receiver distance, $R(\omega)$ is the site response, $I(\omega)$ is the instrument response and $G(\Delta)$ is the path geometric spreading. t^* is given by

$$t^* = \int \frac{Q^{-1}(s)}{\beta(s)} ds, \tag{2}$$

where s is the ray path and β is the velocity. Thus, t^* is a measurement of the accumulated attenuation along a ray path. The ratio of two amplitude spectra, specifically S and ScS, is then

$$\frac{A_{ScS}(\omega\theta\Delta)}{A_S(\omega\theta\Delta)} = \frac{S_{ScS}(\omega)B_{ScS}(\theta, \Delta)R_{ScS}(\omega)I_{ScS}(\omega)G_{ScS}(\Delta)e^{-\omega t^*_{ScS}/2}}{S_S(\omega)B_S(\theta, \Delta)R_S(\omega)I_S(\omega)G_S(\Delta)e^{-\omega t^*_S/2}}, \tag{3}$$

where subscripts denote quantities for either the S or ScS seismic phase. Because we will measure the spectra of S and ScS on the same seismic recording, the source and instrument terms cancel. If we make the further requirement that S and ScS have similar paths near the source and receiver then the source radiation and site term differences between S and ScS are negligible and the logarithmic amplitude of the spectral ratio becomes

$$\ln \frac{|A_{ScS}(\omega, \theta, \Delta)|}{|A_S(\omega, \theta, \Delta)|} = \ln \frac{|G_{ScS}(\Delta)|}{|G_S(\Delta)|} - \frac{\omega}{2}(t^*_{ScS} - t^*_S). \tag{4}$$

This is the equation of a line with intercept $\ln(|G_{ScS}(\Delta)|/|G_S(\Delta)|)$ and slope $(\delta t^*_{ScS} - \delta t^*_S)/2$. Thus, the linear slope is proportional to the differential t^* between ScS and S (δt^*_{ScS-S}).

We calculate the amplitude spectra of S and ScS using the multitaper method of Thomson (1982) with three discrete prolate spheroidal sequences, and fit a line through their logarithmic ratio to compute δt^*_{ScS-S}. Fig. 1 gives an example of a spectral ratio measurement. Past studies using the spectral ratio method with shear waves have used different bandwidths over which to compute the least-squares fit, e.g. 0.005–0.06 Hz (Jordan & Sipkin 1977; Lay & Wallace 1983), 0.001–0.083 Hz (Flanagan & Wiens 1994), 0.02–0.1 Hz (Bhattacharyya *et al.* 1996) and 0.01–0.15 Hz (Fisher *et al.* 2003). Two important considerations in defining a frequency window for spectra ratios are (i) proper inclusion of the dominant energy in the seismic phases of interest and (ii) exclusion of noise and/or additional spurious or undesired arrivals. With these considerations in mind for S and ScS recorded by broadband instruments, we chose to make the δt^*_{ScS-S} measurement in the 0.02–0.12 Hz frequency range.

An important assumption in the spectral ratio method to calculate differential t^* is that Q is independent of frequency. However, in an anelastic medium, Q is a function of frequency (Anderson 2007). Q^{-1} is often modelled with a power-law dependence on frequency

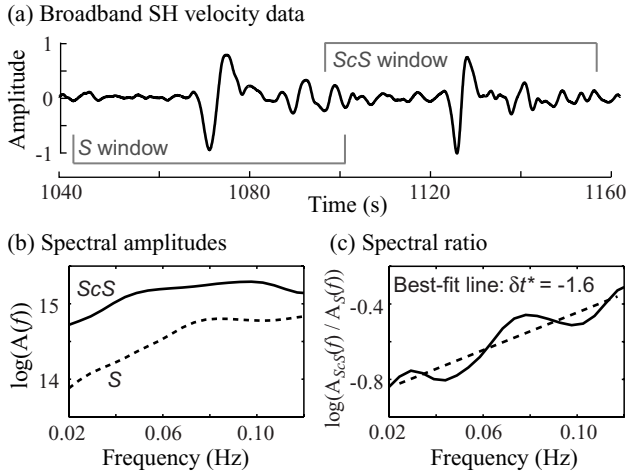

Figure 1. The spectral ratio method to calculate differential t^*. (a) Tangential component of broadband velocity of *S* and *ScS* from event 19971128 recorded at station PLM (distance = 65.5°). The windows of the *S* and *ScS* phases used in the spectral ratios are given. (b) The logarithmic spectral amplitudes of *S* (dahsed line) and *ScS* (solid line). (c) The ratio of the logarithmic spectral amplitudes of *ScS* to *S* (solid line) and the least-squares best fit (dashed line). δt^*_{ScS-S} is calculated to be –1.6 s for this example.

ω of order α and an Arrhenian dependence on temperature T,

$$Q^{-1}(\omega, \mathrm{T}) \sim \omega^{-\alpha} e^{-\alpha \mathrm{E/PR}} \tag{5}$$

(Schoeck *et al.* 1964), where E is the activation energy of the material and R is the universal gas constant. Laboratory measurements by Jackson *et al.* (2010) found α to be approximately 0.25 at frequencies between 0.01 and 1 Hz, however, relating these measurements to the mantle is not straightforward because of uncertainties in the behaviour of mantle material at high pressures and temperatures. Early seismological studies showed that Q is effectively frequency independent ($\alpha \sim 0$) at periods greater than 10 s (Sipkin & Jordan 1979; Burdick 1985). However, frequency independent Q at low frequencies may be because of scattering losses (van der Baan 2002) or partial melting (Faul *et al.* 2004). More recently, Q has been found to have a dependence on ω ($\alpha \approx 0.2$–0.4) for low frequency body waves (Cheng & Kennett 2002; Shito *et al.* 2004), and on the basis of normal mode and surface wave attenuation measurements, Lekic *et al.* (2009) argue that $\alpha \approx 0.3$ in the frequency range 0.005–0.02 Hz. However, frequency independence of Q must be assumed in order for eq. (4) to be valid, where the implicit assumption made in past spectral ratio studies is that the dependence of Q on frequency is negligible for the small bandwidths of short seismic periods under investigation. In fact, using the equations for frequency-independent and frequency-dependent Q given in Müller (1983), we find the spectral ratio of frequency-dependent attenuated seismic phases in the range 0.02–0.12 Hz calculated under an assumption of frequency independence gives a percent error in δt^* of 200α.

2.2 Instantaneous frequency matching

The complex signal $Y(t)$ is given by

$$Y(t) = y(t) + iy^*(t). \tag{6}$$

(Gabor 1946), where $y(t)$ is the real seismic signal and the imaginary part $y^*(t)$ is the quadrature trace. We can express $y(t)$ as a harmonic signal in terms of a time-dependent amplitude $a(t)$ and phase θ (t)

$$y(t) = a(t)\cos\theta(t), \tag{7}$$

then the quadrature signal is

$$y^*(t) = a(t)\sin\theta(t). \tag{8}$$

Eqs (7) and (8) are conjugate harmonic pairs and $y^*(t)$ can be obtained via the Hilbert transform of $y(t)$. The complex signal can now be defined in terms of complex exponentials

$$Y(t) = a(t)e^{i\theta(t)}. \tag{9}$$

Complex seismic trace analysis uses the definition of the complex signal to derive instantaneous attributes. The instantaneous amplitude, or envelope trace, $a(t)$ is

$$a(t) = \sqrt{y(t)^2 + y^*(t)^2}. \tag{10}$$

The instantaneous phase $\theta(t)$ is

$$\theta(t) = \tan^{-1}\left(\frac{y^*(t)}{y(t)}\right) \tag{11}$$

(Goodman 1960). The instantaneous frequency $f(t)$ is the time rate of change of the instantaneous phase

$$f(t) = \frac{1}{2\pi}\frac{d}{t}\theta(t) \tag{12}$$

(Taner *et al.* 1979). In practice $f(t)$ is calculated by taking the derivative of the arctangent function in eq. (11), which results in

$$f(t) = \frac{1}{2\pi}\frac{y(t)\frac{d}{dt}y^*(t) - y^*(t)\frac{d}{dt}y(t)}{y^2(t) + y^{*2}(t)}. \tag{13}$$

The physical meaning of instantaneous phase and frequency are difficult to extract from eqs (11) and (12), but they are analogous to properties in Fourier analysis. Saha (1987) showed that the instantaneous frequency of a seismic phase at its envelope peak is equal to its average Fourier spectral frequency weighted by its amplitude spectrum $A(f)$, or

$$f(t_{peak}) = \frac{\int_0^\infty f A(f) df}{\int_0^\infty A(f) df}, \tag{14}$$

$f(t)$ can be weighted to obtain a more stable measurement. We weight instantaneous frequency by instantaneous power, or amplitude squared, within a running time window W so that $f(t)$ takes the form

$$f(t) = \frac{\int_{t-W/2}^{t+W/2} f(t)a^2(t)dt}{\int_{t-W/2}^{t+W/2} a^2(t)dt} \tag{15}$$

(Saha 1987; Matheney & Nowack 1995; Barnes 2000).

Matheney & Nowack (1995) developed the method of instantaneous frequency matching to calculate δt^* between an observed and reference seismic pulse. The method operates on the assumption that as a seismic phase propagates through an anelastic medium, the dominant period of that phase decreases. By measuring the difference in dominant period between an observed and reference pulse, the differential attenuation can be inferred. The instantaneous frequency of the observed waveform $f_{\mathrm{obs}}(t)$ and the time where the envelope of the observed pulse is a maximum (t_{obs}) are calculated. The reference pulse is then attenuated until the instantaneous frequency $f_{\mathrm{ref}}(t)$ at its envelope peak t_{ref} matches $f_{\mathrm{obs}}(t_{\mathrm{obs}})$. Attenuation of the reference pulse is done in the frequency domain with the causal attenuation operator

$$D(\omega) = e^{\frac{-\omega}{2}t^*\left(1-\frac{2i}{\pi}\ln\frac{\omega}{\omega_r}\right)} \tag{16}$$

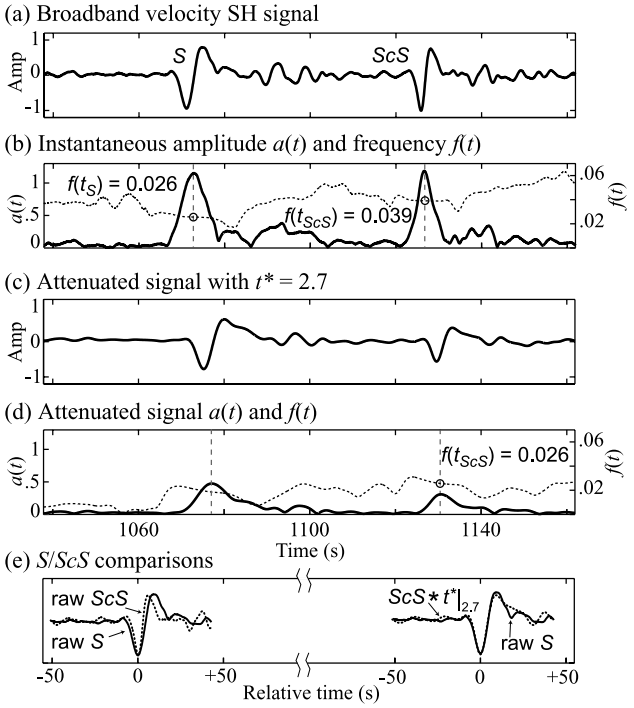

Figure 2. The instantaneous frequency method to calculate differential t^*. (a) Same trace as Fig. 1(a). (b) The trace envelope (solid line) and instantaneous frequency (dashed line). The instantaneous frequency at the envelope peaks (vertical dashed lines) of S ($f(t_S)$) and ScS ($f(t_{ScS})$) are given. (c) The trace after convolution with a t^* operator equal to 2.7 s. (d) The trace envelope (dashed line) and instantaneous frequency (solid line) after attenuation. The instantaneous frequency at the envelope peak ScS is now equal to $f(t_S)$. (e) Comparison of raw and attenuated traces, where the ScS amplitude after convolution with a t^* operator = 2.7 is normalized to the maximum S amplitude. t^* is negative because $f(t_{ScS})$ is greater than $f(t_S)$.

(Müller 1983), where t^* is the same as eq. (3) and ω_r is the reference frequency. A choice of ω_r between 0.1 and 1 Hz has a negligible effect on the calculation, and we choose a value of 1 Hz. The value of t^* in eq. (16) that attenuates the reference pulse to cause a match between $f_{\mathrm{obs}}(t_{\mathrm{obs}})$ and $f_{\mathrm{ref}}(t_{\mathrm{ref}})$ is the differential t^* between the two pulses. One benefit of the instantaneous frequency matching method is that there is no assumption of constant Q (Dasios *et al.* 2001).

We alter the method slightly to calculate δt^*_{ScS-S}, an example of which is shown in Fig. 2. Now the seismic phases are on the same trace (observed and reference are both observed phases), and either phase could be more attenuated than the other. Therefore, we calculate $f(t)$ of the waveform (dashed line in Fig. 2b) and find its value at the envelope peak of S and ScS, where the time of these peaks are t_S and t_{ScS}, respectively (vertical dashed lines in Fig. 2b). If $f(t_{ScS})$ is smaller than $f(t_S)$, as would be expected in an homogeneous Earth (because the path length of ScS is greater than S), we attenuate the trace until the instantaneous frequency at the envelope peak of S is equal to $f(t_{ScS})$. An example of this attenuated trace is shown in Fig. 2(c) and its associated $f(t)$ with envelope peaks are given in Fig. 2(d). The value of t^* in the attenuation operator (eq. 16) that accomplishes this equalization is δt^*_{ScS-S} (Fig. 2). If $f(t_S)$ is smaller than $f(t_{ScS})$, we attenuate the trace until the instantaneous frequency at the envelope peak of ScS is equal to $f(t_S)$. This is the case for the example given in Fig. 2, where panel (d) shows that after attenuating the trace in panel (a) with a negative t^* operator the result is the trace in panel (c) where the $f(t_{ScS})$ (shown in Fig. 2d) equals the original $f(t_S)$ (shown in Fig. 2b). The value of t^* in the attenuation operator that accomplishes this is $-\delta t^*_{ScS-S}$. Fig. 2(e) compares S and ScS before and after attenuating the ScS trace with a $t^* = 2.7$, and in this case $\delta t^*_{ScS-S} = -2.7$. Note that the amplitudes of the phases have been normalized for presentation purposes. We solve for t^* with

$$t^*_{new} \cong t^*_{old} + \frac{f(t_{phase1}) - f_{atten}(t_{phase2})}{df_{atten}(t_{phase2})/dt^*} \tag{17}$$

(Matheney & Nowack 1995), where t^*_{old} is the value of t^* from the previous calculation, $f(t_{\mathrm{phase1}})$ is the initially smaller value of either $f(t_{ScS})$ or $f(t_S)$, $f_{\mathrm{atten}}(t_{\mathrm{phase2}})$ is the instantaneous frequency of the attenuated trace at the initially greater of either $f(t_{ScS})$ or $f(t_S)$, $\mathrm{d}f_{\mathrm{atten}}(t_{\mathrm{phase2}})/\mathrm{d}t^*$ *i*s the change of instantaneous frequency because of a change in t^* (this value is approximated with a finite difference) and t^*_{new} is the updated t^* value. The calculation is applied iteratively until $f(t_{\mathrm{phase1}}) - f_{\mathrm{atten}}(t_{\mathrm{phase2}})$ is less than 0.01 mHz, after which t^*_{new} is δt^*_{ScS-S}. This iterative procedure to find the best t^* could be replaced with a grid search over a range of t^* for the one that minimizes $f(t_{\mathrm{phase1}}) - f_{\mathrm{atten}}(t_{\mathrm{phase2}})$.

2.3 Method comparison and analysis

Two types of synthetic waveforms are constructed to compare the instantaneous frequency matching and spectral ratio methods. In the first, the causal attenuation operator described by eq. (16) is inverse Fourier transformed, time shifted and convolved with a delta function at the arrival time of S and ScS at every 1° in distance between 40° and 80° (event depth of 100 km), where the reference period is 12 s. The t^* and arrival time values are appropriate for phases traversing the 1 Hz Preliminary Reference Earth Model (PREM; Dziewonski & Anderson 1981).

White (1992) showed that the variance in spectral ratios is inversely proportional to the time-window length used in the spectral amplitude calculation. Ideally, the time window should be at least several times larger than the dominant period (T) of the phase of interest. This is not always possible, because as the window size increases, so too does the amount of noise and the possibility of analysing phases other than the phase of interest. We test windows that are three, five and seven times greater than the period of the phase ($3T$, $5T$ and $7T$, respectively), and centred on the maximum envelope amplitude of the phase (Fig. 3a). When the window is too small, as is the case with a length of $3T$, not all the energy of the phase is accounted for in the calculation. If the window is too large, as is the case with $7T$, the neighbouring ScS contaminates the S window, and vice versa. Of the three window lengths, $5T$ allows for an accurate calculation of δt^* out to a distance of approximately 70°, a distance where S or ScS began to enter the $5T$ time window centred on the other phase, which skews the measurement. The S and ScS broadband data we analyse have a dominant period of approximately 12 s, so we will use 60-s time windows in the spectral ratio calculation.

We also examine the effect of the size of the weighting window W in eq. (15) on instantaneous frequency. As W increases, the variance in instantaneous frequency is reduced and its measurement stabilized (White 1991). We test values of W that are 50, 75 and 100 per cent of the period of the phase (Fig. 3b). The size of W does not have much effect on the t^* measurement, and as in other studies (Claerbout 1992; Matheney & Nowack 1995; Barnes 2000) we will use a weighting window W that is the size of the dominant period of the phase of interest (100 per cent of T), or, as stated earlier, 12 s. After consideration of the time window in the spectral ratio method and the weighting window in instantaneous frequency matching

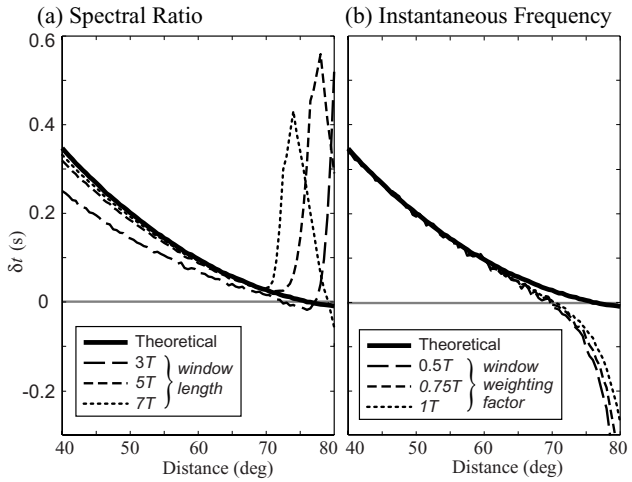

Figure 3. Theoretical tests of the (a) spectral ratio and (b) instantaneous frequency method for determination of δt^*_{ScS-S} on synthetic traces with a dominant period T of 12 s. (a) The effect of window length as a function of T. (b) The effect of weighting window as a function of T. The black line is theoretical δt^*_{ScS-S}.

method, both methods do very well in returning the theoretical δt^*_{ScS-S} at distances less than 70° (Fig. 3). Beyond this distance, *S* and *ScS* are too close in time, causing inaccurate measurements from both methods.

Random noise that has been filtered with a second-order bandpass Butterworth filter between 1 and 100 s is added to the synthetic waveforms to investigate the relationship between signal-to-noise ratio (SNR) and method performance. SNR is measured by taking the rms of the waveform between the beginning of the *S* arrival and 20 s after the *ScS* arrival (an interval of length T_{sig} s) and dividing that value by the rms of the waveform for T_{sig} s before the beginning of the *S* arrival. Fig. 4 shows that as the SNR decreases, the rms of all δt^*_{ScS-S} measurements (for the 31 distances between 40° and

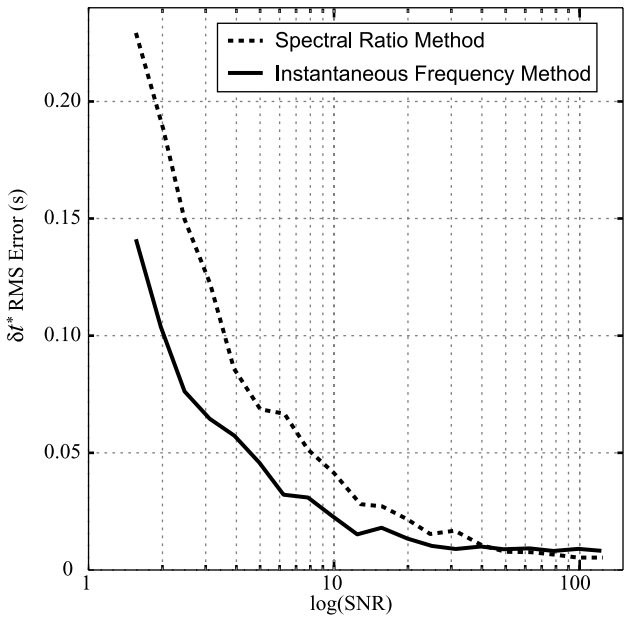

Figure 4. The rms of δt^*_{ScS-S} calculated for the same synthetics as is used in the analysis presented in Fig. 3 (31 traces at 1° distance intervals between 40° and 70°) at different magnitudes of SNR by the spectral ratio method (dashed line) and the instantaneous frequency matching method (solid line).

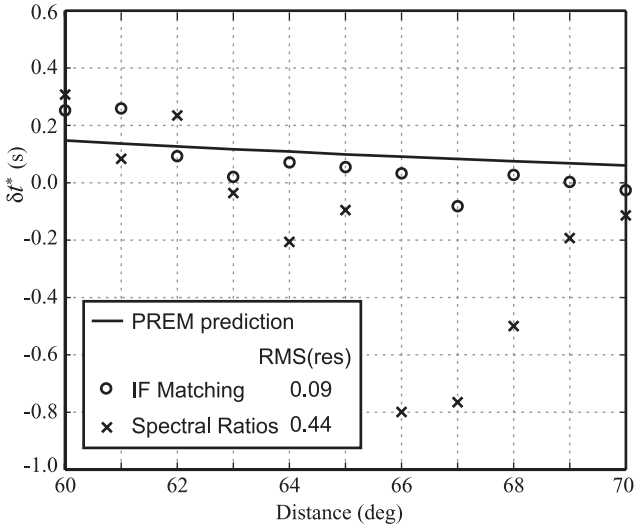

Figure 5. δt^*_{ScS-S} calculated from reflectivity synthetics as a function of distance for an earthquake with a depth of 500 km using the spectral ratio method (crosses) and instantaneous frequency method (circles). The black line is PREM-predicted δt^*_{ScS-S}.

70°) increases for both methods as expected. However, the error in the instantaneous frequency matching method does not increase as rapidly as the spectral ratio method, and the difference in rms error of the methods at an SNR of 1.5 is almost 0.1 s, which is the same order as the theoretical value of δt^*_{ScS-S} for the PREM synthetics in this experiment. Typical studies using teleseismic *S* and *ScS* make measurements on data with an SNR of 3 and greater, where there is still a significant improvement using the instantaneous frequency matching method.

Another type of synthetic waveform is created using the 1-D reflectivity method (Fuchs & Müller 1971; Müller 1985), which incorporates frequency-independent attenuation. The whole *SH* wavefield appropriate for an earthquake at 500-km depth recorded at distances between 60° and 70° in the 1 Hz PREM model is made. We restricted our analysis to records recorded at distances between 60° and 70°, because at a distance greater than 70° *S* begins to interfere with *ScS* (Fig. 3), and at a distance less than 60°, the *S* and *ScS* paths diverge greatly in the mantle and the assumption that δt^*_{ScS-S} is because of deep mantle structure is less constrained. An earthquake at a depth of 500 km removes interference of the phases of interest, *S* and *ScS*, by the depth phases, *sS* and *sScS*, and we can examine the effects of other interfering phases on the two differential t^* measurement techniques. Fig. 5 shows that both techniques perform well, but the residuals are much smaller for the instantaneous frequency matching method where the rms of the residuals ($\delta t^*_{theoretical} - \delta t*_{measured}$) is 0.09 s compared with 0.44 s for the spectral ratio method. From the results of these synthetic tests, we conclude that the instantaneous frequency matching method performs better than the spectral ratio method in the presence of noise and interfering phases. Dasios *et al.* (2001) came to similar conclusions using compressional waves in the borehole environment.

3 REGIONAL STUDY APPLICATION

We apply the instantaneous frequency matching method to 54 seismic traces that sample the lowermost mantle beneath Central America and the Cocos plate to estimate δt^*_{ScS-S}. Data are from three South American earthquakes with magnitudes greater than 6.0 and

Table 1. Event and station summary.

Event (YYYYMMDD)	Latitude	Longitude	Depth (km)	Mag (Ms)	Station	Latitude	Longitude	Elevation (m)	Distance (deg)
19940110	−13.34	−69.45	596	6.90	CMB[a]	38.03	−120.39	697	69.90
					SAO[a]	36.76	−121.45	317	69.84
19971128	−13.74	−68.79	586	6.70	BZN[b]	33.49	−116.67	1301	65.48
					DGR[c]	33.65	−117.01	609	65.80
					FRD[b]	33.49	−116.60	1164	65.44
					GSC[c]	35.30	−116.81	954	66.68
					KCC[a]	37.32	−119.32	888	69.52
					LVA2[b]	33.35	−116.56	1435	65.32
					MWC[c]	34.22	−118.05	1696	66.84
					OSI[c]	34.61	−118.72	706	67.52
					PAS[c]	34.15	−118.17	314	66.87
					PFO[b]	33.61	−116.46	1259	65.41
					PHL[c]	35.41	−120.55	351	69.19
					PKD[a]	35.95	−120.54	583	69.50
					PLM[c]	33.35	−116.86	1660	65.52
					SND[a]	33.55	−116.61	1358	65.48
					ALP[c]	34.69	−118.30	753	61.35
					BBR[c]	34.26	−116.92	2069	60.17
20021012	−8.30	−71.74	534	6.90	BDM[a]	37.95	−121.87	220	65.56
					BFS[c]	34.24	−117.66	1296	60.65
					BRK[a]	37.87	−122.26	49	65.78
					CCC[c]	35.52	−117.36	670	61.21
					CGO[c]	36.55	−117.80	2795	62.10
					CHF[c]	34.33	−118.03	1594	60.96
					CIA[c]	33.40	−118.41	467	60.69
					CLC[c]	35.82	−117.60	775	61.53
					CVS[a]	38.35	−122.46	295	66.17
					DEC[c]	34.25	−118.33	519	61.12
					FARB[a]	37.70	−123.00	−18	66.18
					FIG[c]	34.73	−119.99	945	62.52
					FUR[c]	36.47	−116.86	−37	61.44
					GR2[c]	34.12	−118.30	316	61.02
					GSC[c]	35.30	−116.81	1000	60.71
					HEC[c]	34.83	−116.33	920	60.12
					JRC[c]	35.98	−117.81	1452	61.77
					JRSC[a]	37.40	−122.24	70	65.51
					JVA[c]	34.37	−116.61	904	60.03
					KCC[a]	37.32	−119.32	888	63.54
					KCPB[c]	39.69	−123.58	1261	67.63
					LGU[c]	34.11	−119.07	416	61.54
					LRL[c]	35.48	−117.68	1340	61.39
					MPM[c]	36.06	−117.49	1839	61.61
					MTP[c]	35.48	−115.55	1588	60.00
					ORV[a]	39.55	−121.50	335	66.22
					PHL[c]	35.41	−120.55	355	63.27
					PKD[a]	35.95	−120.54	583	63.57
					RPV[c]	33.74	−118.40	107	60.88
					RVR[c]	33.99	−117.38	266	60.32
					SLA[c]	35.89	−117.28	1174	61.37
					SMM[c]	35.31	−120.00	599	62.85
					THE[c]	35.29	−118.42	846	61.77
					VCS[c]	34.48	−118.12	991	61.11
					WBS[c]	35.54	−118.14	1927	61.73
					YBH[a]	41.73	−122.71	1060	68.20

[a]Berkeley Digital Seismic Network (Berkeley Seismological Laboratory).
[b]Anza Seismic Network (Institute of Geophysics and Planetary Physics).
[c]Southern California Seismic Network (Seismological Laboratory at Caltech).

depths below 400 km, which were recorded by stations in California of the Berkeley Digital Seismic Network, Southern California Seismic Network and Anza Seismic Network (Table 1). We rotated traces to the great-circle reference frame to obtain transverse components of motion, keeping records with SNR greater than 1.4 for which more than five stations recorded the same event so that we could reliably identify *S* and *ScS*. The SNR cut-off was chosen to maximize the number of data for a more robust analysis. An

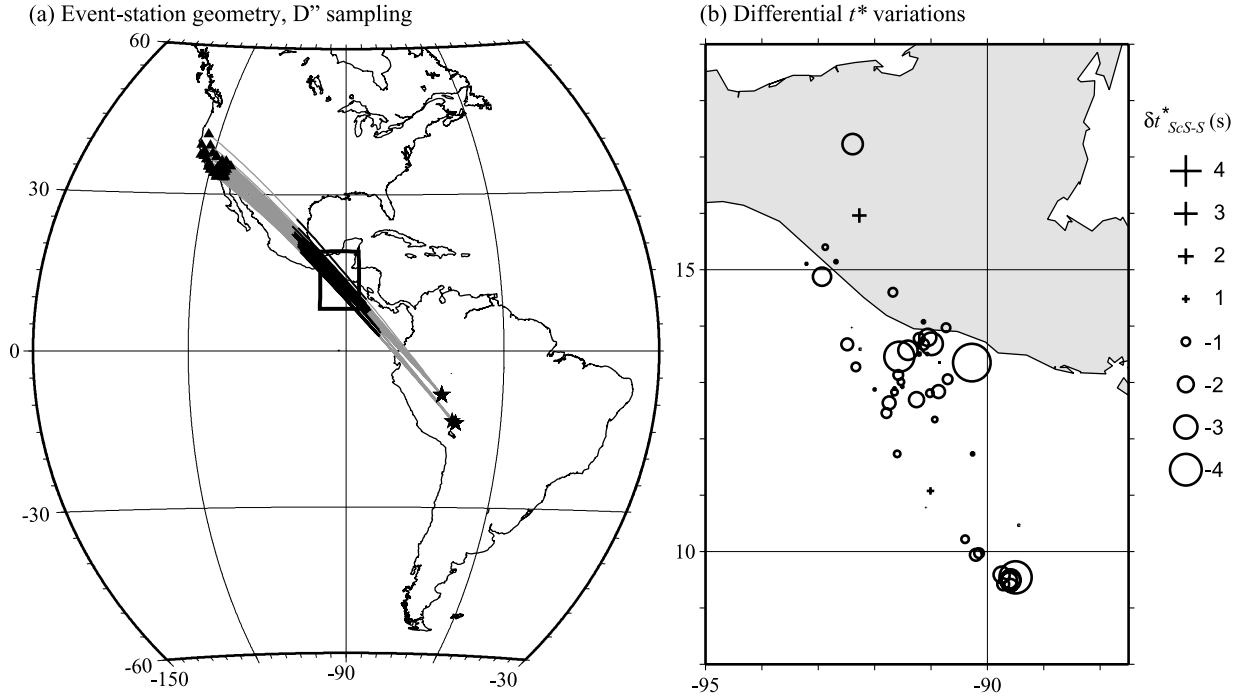

Figure 6. Lateral variations in δt^*_{ScS-S}. (a) Station (triangle)-event (star) and great-circle ray path (grey line) geometry for our data set. The dark portion of the ray path is where *ScS* traverses a 300 km thick D″, as calculated with the PREM velocity model. (b) δt^*_{ScS-S} plotted at *ScS* reflection points for the region outlined in (a).

advantage of the instantaneous frequency matching method is that low-SNR data can be analysed with less error than other methods (Fig. 4). The choice of a greater SNR cut-off does not significantly affect the δt^*_{ScS-S} patterns in this study. For these source depths, *sS* never arrived less than 50 s after *ScS*, thus precluding contamination of the instantaneous frequency measurement. For the reasons stated above, we restrict our analyses to records with distances between 60° and 70°. It should be noted that, similar to many other lower mantle differential studies, the data set suffers from limited azimuthal sampling (Fig. 6a).

δt^*_{ScS-S} is plotted at the *ScS* reflection point (calculated for PREM) in Fig. 6(b) to aid in spatial analysis of lateral attenuation heterogeneity. Most of our δt^*_{ScS-S} measurements are negative (circles), indicating that the dominant period of *ScS* is greater than *S*. The minimum value measured is –4.6 s. There are some positive values of δt^*_{ScS-S} and the maximum is 1.8 s.

4 DISCUSSION

A first approach in interpreting δt^*_{ScS-S} is that positive values result from stronger attenuation in the deepest mantle (thus preferentially broadening *ScS*), whereas negative values reflect the opposite case, a broadening of the *S* wave from stronger attenuation at depths where the *S* wave is bottoming. Attributing our largest positive δt^*_{ScS-S} values (∼1.8 s) to anomalous attenuation structure in a 300-km thick D″ layer results in a very low Q_μ (high attenuation), roughly 30 per cent of the PREM value, or approximately 90. (vertical dashed line in Fig. 7). This value of Q_μ is close to the value used in 1-D models of the highly attenuating asthenosphere (Resovsky *et al.* 2005). It is noteworthy that Fisher *et al.* (2003) observe even larger positive δt^*_{ScS-S} values (with a mean of 2.6 s) to the east of our study region, beneath Central America and the Caribbean, which they model as a high attenuation D″ with $Q_\mu = 70$.

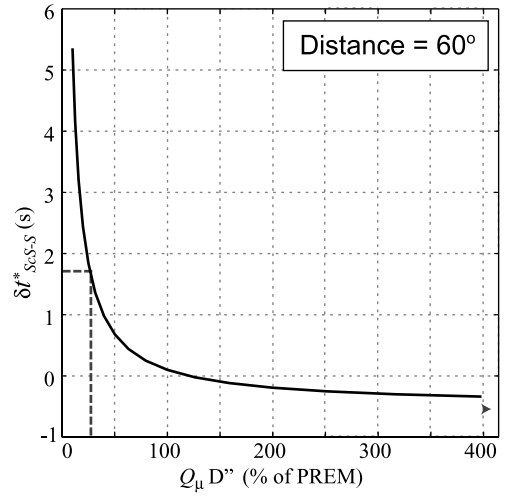

Figure 7. δt^*_{ScS-S} at a distance of 60° calculated with the PREM shear Q (Q_μ) model, where Q from a depth of 2591 km to the CMB (300 km thick D″) is varied as a percentage of PREM lower mantle Q ($Q = 312$). The dashed line shows that the most positive δt^*_{ScS-S} measured in this study could be modelled with a D″ that is 30 per cent of PREM ($Q_\mu = 90$).

Conversely, mapping the largest negative δt^*_{ScS-S} (–4.6 s) to a 300 km thick D″ layer results in unrealistically high Q_μ. Therefore, δt^*_{ScS-S} less than –1 s must in all likelihood be because of something other than D″ attenuation structure. Tanaka & Hamaguchi (1992) measured negative δt^*_{ScS-S} values as low as –4 s in their study of lower mantle heterogeneity beneath Africa. They suggest that this is caused by a mid-mantle Q_μ anomaly between 100 and 200 km beneath Africa. Negative δt^*_{ScS-S} can also be because of elastic effects that would cause *S* pulse broadening, thereby lowering the instantaneous frequency of the *S* phase relative to *ScS* and imparting an effective t^* to the differential

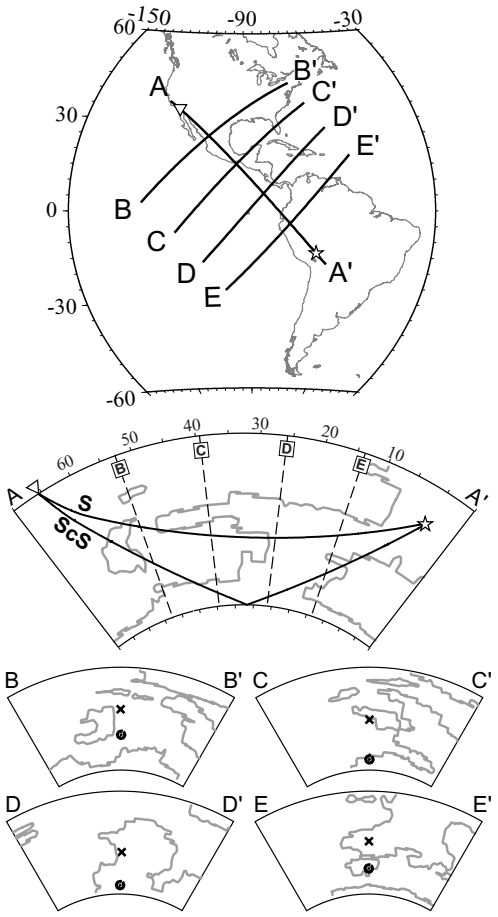

Figure 8. Velocity heterogeneity sampled by the *S* and *ScS* ray paths in this study. (a) Map showing event (star)-station (inverted triangle) geometry and the transects of the cross-sections plotted. This is also the cross-section used for waveform modelling. The A–A′ cross-section shows the *S* (upper) and *ScS* (lower) ray paths and depths at which they pierce the other transects (black vertical lines). Every cross-section plots the 0.2 per cent fast shear velocity contour (gray lines) of the tomography model, TXBW (Grand 2002). Cross-sections B–B′ through E–E′ show the piercing location of *S* (cross) and *ScS* (circle). The structure outlined by contours in the mid-mantle could be slab remnants.

measurement. Candidates for such effects are focusing/defocusing and scattering of the wavefield because of velocity heterogeneity (Woodhouse & Wong 1986; Lee *et al.* 2003), multipathing and diffraction because of a low-velocity slab (Vidale 1987; Cormier 1989; Igel *et al.* 2002) and seismic anisotropy (Kendall & Thomson 1993). Indeed, Fig. 8 shows ray paths of our data that traverse a region that has strong velocity heterogeneity in the lower mantle (e.g. Tkalčić & Romanowicz 2002; Garnero & Lay 2003; Hung *et al.* 2005) and mid-mantle with the possible remains of the ancient Farallon slab (e.g. Bokelmann & Silver 1993; Grand *et al.* 1997; Grand 2002), and strong seismic anisotropy (Rokosky *et al.* 2004). Core–mantle boundary topography can also cause focusing/defocusing of core-reflected phases (Kampfmann & Muller 1989). Emmerich (1993) shows that the effect of topography on *ScS* is much less than *PcP* at the distances and frequencies considered in this study and that wave front healing removes most of the effect so that its magnitude has an insignificant contribution to the results presented here.

Table 2. Data subset of 19971128.

Station	Distance (deg)	δt^*_{ScS-S} (s)
DGR	65.80	−1.9
RDM	65.68	−2.1
KNW	65.65	−2.3
CRY	65.57	−2.7
WMC	65.54	−2.9
PLM	65.52	−2.7
SND	65.48	−1.8
BZN	65.48	−2.0
FRD	65.44	−1.6

To explore possible effects of elastic heterogeneity on our δt^*_{ScS-S} measurements, we create synthetic *SH* waveforms for a cross-section through a tomographically derived 3-D shear velocity heterogeneity model using an axisymmetric finite-difference algorithm, SHaxi (Thorne *et al.* 2007). This method allows us to characterize mantle heterogeneity in the plane of propagation, but because of the cylindrical symmetry, these structures continue in and out of the great-circle plane (thus, this approach is often considered 2.5-D). We measure δt^*_{ScS-S} on synthetic waveforms that have propagated through the 3-D velocity tomography model TXBW (Grand 2002) with station-event geometry exactly as a subset of our data set (path A–A′ in Fig. 8 with stations given in Table 2), and compare the values with those propagated through the 1-D PREM velocity model. δt^*_{ScS-S} measured from the TXBW synthetics are only slightly larger than values for the PREM synthetics (which, as expected, are near 0 s) and the average difference between of the two synthetic measurements ($\delta t^*_{\text{residual}}$) is approximately 0.3 s (crosses in Fig. 9). Not only is the effective δt^*_{ScS-S} calculated from the TXBW synthetics small, but it is also positive, and therefore cannot account for our large negative δt^*_{ScS-S} observations. However, the strength of velocity heterogeneity in TXBW is probably underestimated because of the smoothing imparted in the inversion process. Zhou & Chen (1995) showed that the waveform effects because of a slab having a 2 per cent increase in V_S compared to the surrounding mantle (as is imaged in tomography models) are very difficult to detect compared to a slab with a 10 per cent V_S contrast. Future work should consider realistic 3-D subducted slab geometries with stronger velocity contrasts. Also, true wave propagation through 3-D (as opposed to 2.5-D) is necessary to better assess possible out of great-circle plane multipathing (e.g. Helmberger & Ni 2005) or diffractions (Cormier 1989) which may contribute to *S*-wave broadening.

Seismic anisotropy in the uppermost mantle beneath the Californian seismic stations (Polet & Kanamori 2002) may affect our *SH* observations, and therefore lead to biases in our measurements. We investigate such effects through a particle motion analysis on the same subset of our data set as before (Table 2) to find the best-fitting splitting parameters (split time dt and fast azimuth ϕ), which yield the most nearly singular covariance matrix and therefore the most linear particle motion (Silver & Chan 1991). We then correct the traces by rotating to ϕ, time shifting by –dt and then rotating back to the great-circle reference frame. δt^*_{ScS-S} measurements after correction for seismic anisotropy are slightly different from measurements made without consideration of anisotropy. The change after correction is both positive and negative, with an average difference between corrected and uncorrected (observed) measurements (δt^* residual) of 0.25 s (circles in Fig. 9). Thus, we estimate that our δt^*_{ScS-S} contain error on the order of several tenths of a second, which should not significantly affect the trend or

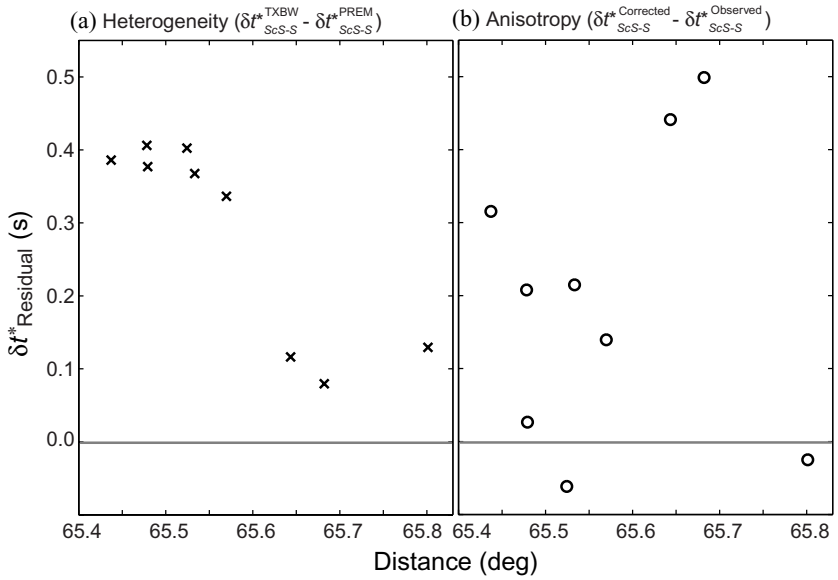

Figure 9. Analysis of velocity heterogeneity and anisotropy effects on δt^*_{ScS-S} measurements. The crosses are differences in measured δt^*_{ScS-S} between synthetics incorporating the velocity heterogeneity of Grand (2002) and PREM-derived synthetics, where the event-station geometry is the same as the data subset in Table 2. The circles are differences in measured δt^*_{ScS-S} between observations that have been corrected for anisotropy and those that have not.

amplitudes in Fig. 6, as this is a small percentage error for the largest anomalies.

5 CONCLUSION

The measurement of differential t^* between *S* and *ScS* in the presence of noise and interference with other seismic arrivals is more accurately calculated with the instantaneous frequency matching method than the spectral ratio method. We test the method on a small data set that samples a region of the lower mantle beneath western Central America and the Cocos plate, and find significantly negative δt^*_{ScS-S}, as low as –4.6 s (i.e. *S* more attenuated than *ScS*). We show that the magnitude of the negative δt^*_{ScS-S} cannot solely be because of a D″ attenuation anomaly, and hence structure along the *S*-wave path must be taken into consideration. We investigate the effects of long wavelength elastic heterogeneity and upper-mantle seismic anisotropy on the measurements in an attempt to better understand effective versus intrinsic attenuation contributions to our data. We find that, although elastic and anisotropic effects are important, the models tested here do not reproduce the large negative δt^*_{ScS-S} values. We note, however, that we may have underestimated the magnitude of δt^*_{ScS-S} because of unaccounted for effects of a possibly stronger slab signature in the mid-lower mantle, and/or 3-D wave propagation effects. We conclude that the instantaneous frequency matching method is a viable type of differential attenuation analysis, and when used in conjunction with other lower mantle probes can be a powerful tool in the exploration of the deep earth.

ACKNOWLEDGMENTS

This work has benefited from insightful discussions with T. Lay and V. Cormier. Broadband waveform data was collected from the Berkeley Seismological Laboratory, Southern California Earthquake Data Center and IRIS. Most signal analysis was done with SAC2000 (Goldstein *et al.* 1999), ray path analysis was aided by the TauP Toolkit (Crotwell *et al.* 1999) and figures were made using GMT (Wessel & Smith 1998). This research was partially supported by NSF grant EAR-0135119. We thank the Center for High Performance Computing at the University of Utah for use of their supercomputing facilities. This work performed under the auspices of the U.S. Department of Energy by Lawrence Livermore National Laboratory under Contract DE-AC52–07NA27344.

REFERENCES

Anderson, D.L., 2007. *The New Theory of the Earth,* University Press, Cambridge.

Anderson, D.L. & Archambeau, C., 1964. Anelasticity of earth, *J. geophys. Res.,* **69,** 2071–2078.

Anderson, D.L. & Hart, R.S., 1978. *Q* of the earth, *J. geophys. Res.,* **83,** 5869–5882.

Barnes, A.E., 2000. Weighted average seismic attributes, *Geophysics,* **65,** 275–285.

Bath, M., 1974. *Spectral Analysis in Geophysics,* Elsevier Scientific Publishing, New York, NY.

Bhattacharyya, J., 1998. Comparison between time-domain and frequency-domain measurement techniques for mantle shear-wave attenuation, *Pure appl. Geophys.,* **153,** 399–417.

Bhattacharyya, J., Masters, G. & Shearer, P., 1996. Global lateral variations of shear wave attenuation in the upper mantle, *J. geophys. Res.,* **101,** 22273–22290.

Bokelmann, G.H.R. & Silver, P.G., 1993. The Caribbean anomaly: short wavelength lateral heterogeneity in the lower mantle, *Geophys. Res. Lett.,* **20,** 1131–1134.

Burdick, L.J., 1985. Estimation of the frequency-dependence of *Q* from ScP and ScS phases, *Geophys. J. R. astr. Soc.,* **80,** 35–55.

Cheng, H.X. & Kennett, B.L.N., 2002. Frequency dependence of seismic wave attenuation in the upper mantle beneath the Australian region, *Geophys. J. Int.,* **150,** 45–57.

Claerbout, J.F., 1992. *Earth Soundings Analysis: Processing Versus Inversion,* Blackwell Scientific Publications, Boston.

Cormier, V.F., 1982. The effect of attenuation on seismic body waves, *Bull. seism. Soc. Am.,* **72,** S169–S200.

Cormier, V.F., 1989. Slab diffraction of s-waves, *J. geophys. Res.,* **94,** 3006–3024.

Crotwell, H.P., Owens, T.J. & Ritsema, J., 1999. The TauP toolkit: flexible seismic travel-time and ray-path utilities, *Seism. Res. Lett.,* **70,** 154–160.

Dalton, C.A. & Ekstrom, G., 2006. Global models of surface wave attenuation, *J. geophys. Res.,* **111**(B10), 5317, doi:10.1029/2005JB003.

Dasios, A., Astin, T.R. & C. McCann, 2001. Compressional-wave *Q* estimation from full-waveform sonic data, *Geophys. Prospect.,* **49,** 353–373.

Durek, J.J. & Ekstrom, G., 1996. A radial model of anelasticity consistent with long-period surface-wave attenuation, *Bull. seism. Soc. Am.,* **86,** 144–158.

Dziewonski, A.M. & Anderson, D.L., 1981. Preliminary reference earth model, *Phys. Earth planet. Inter.,* **25,** 297–356.

Emmerich, H., 1993. Theoretical-study on the influence of CMB topography on the core reflection ScS, *Phys. Earth planet. Inter.,* **80,** 125–134, doi:10.1016/0031-9201(93)90043-9.

Engelhard, L., 1996. Determination of seismic-wave attenuation by complex trace analysis, *Geophys. J. Int.,* **125,** 608–622, doi:10.1111/j.1365-246X.1996.tb00023.x.

Faul, U.H., Gerald, J.D.F. & Jackson, I., 2004. Shear wave attenuation and dispersion in melt-bearing olivine polycrystals: 2. microstructural interpretation and seismological implications, *J. geophys. Res.,* **109,** B06202, doi:10.1029/2003JB002407.

Fisher, J.L., Wysession, M.E. & Fischer, K.M., 2003. Small-scale lateral variations in D′′ attenuation and velocity structure, *Geophys. Res. Lett.,* **30,** 1811–1814.

Flanagan, M.P. & Wiens, D.A., 1994. Radial upper mantle attenuation structure of inactive back arc basins from differential shear wave measurements, *J. geophys. Res.,* **99,** 15469–15486.

Fuchs, K. & Muller, C., 1971. Computation of synthetic seismograms with the reflectivity method and comparison with observations, *Geophys. J. R. astr. Soc.,* **23,** 417–433.

Futterman, W.I., 1962. Dispersive body waves, *J. geophys. Res.,* **67,** 5279–5286.

Gabor, D., 1946. Theory of communication, *J. Inst. Elect. Eng.,* **93,** 429–441.

Gao, J., Yang, S., Wang, D. & Wu, R., 2011. Estimation of quality factor Q from the instantaneous frequency at the envelope peak of a seismic signal, *J. Comput. Acoust.,* **19,** 155–179, doi:10.1142/S0218396x11004390"×11004390.

Garnero, E.J., 2000. Heterogeneity of the lowermost mantle, *Annu. Rev. Earth planet. Sci.,* **28,** 509–537.

Garnero, E.J. & Lay, T., 2003. D′′ shear velocity heterogeneity, anisotropy and discontinuity structure beneath the Caribbean and Central America, *Phys. Earth planet. Inter.,* **140,** 219–242.

Goodman, N.R., 1960. Measuring amplitude and phase, *J. Franklin Inst.,* **70,** 437–450.

Grand, S.P., 2002. Mantle shear-wave tomography and the fate of subducted slabs, *Phil. Trans. R. Soc. Lond., A.,* **360,** 2475–2491.

Grand, S.P., van der Hilst, R.D. & Widyantoro, S., 1997. Global seismic tomography: a snapshot of convection in the Earth, *Geol. Soc. Am. Today,* **7**(4).

Helmberger, D.V. & Ni, S., 2005. Seismic modeling constraints on the South African super plume, in *Earth's Deep Mantle: Structure, Composition, and Evolution,* pp. 134–139, eds van der Hilst, R.D., Bass, J.D., Matas, J. & Trampert, J., American Geophysical Union, Washington, D.C.

Hung, S.H., Garnero, E.J., Chiao, L.Y., Kuo, B.Y. & Lay, T., 2005. Finite frequency tomography of D shear velocity heterogeneity beneath the Caribbean, *J. geophys. Res.,* **110,** 1–20.

Igel, H., Nissen-Meyer, T. & Jahnke, G., 2002. Wave propagation in 3D spherical sections: effects of subduction zones, *Phys. Earth planet. Inter.,* **132,** 219–234.

Jackson, I., 2000. Laboratory measurement of seismic wave dispersion and attenuation: recent progress, in *Earth's Deep Interior: Mineral physics and Tomography from the Atomic to the Global Scale,* pp. 265–289, ed. S.-I. Karato, American Geophysical Union, Washington, D.C.

Jackson, I. & Faul, U.H., 2010. Grainsize-sensitive viscoelastic relaxation in olivine: towards a robust laboratory-based model for seismological application, *Phys. Earth planet. Int.,* **183,** 151–163, doi:10.1016/j.pepi.2010.09.005.

Jordan, T.H. & Sipkin, S.A., 1977. Estimation of attenuation operator for multiple ScS waves, *Geophys. Res. Lett.,* **4,** 167–170.

Kampfmann, W. & Muller, G., 1989. PcP amplitude calculations for a core-mantle boundary with topography, *Geophys. Res. Lett.,* **16,** 653–656, doi:10.1029/GL016i007p00653.

Kanamori, H., 1967. Spectrum of P and PcP in relation to mantle-core boundary and attenuation in mantle, *J. geophys. Res.,* **72,** 559–569.

Karato, S., 1993. Importance of anelasticity in the interpretation of seismic tomography, *Geophys. Res. Lett.,* **20,** 1623–1626.

Karato, S. & Spetzler, H.A., 1990. Defect microdynamics in minerals and solid-state mechanisms of seismic-wave attenuation and velocity dispersion in the mantle, *Rev. Geophys.,* **28,** 399–421.

Kendall, J.M. & Thomson, C.J., 1993. Seismic modeling of subduction zones with inhomogeneity and anisotropy.1. Teleseismic P-wave-front tracking, *Geophys. J. Int.,* **112,** 39–66.

Knopoff, L., 1964. *Q. Rev. Geophys.,* **2,** 625–660.

Kuo, B.Y., Garnero, E.J. & Lay, T., 2000. Tomographic inversion of S-SKS times for shear velocity heterogeneity in D: degree 12 and hybrid models, *J. geophys. Res.,* **105,** 28139–28158.

Lawrence, J.F. & Wysession, M.E., 2006. QLM9: a new radial quality factor (Q_μ) model for the lower mantle, *Earth planet. Sci. Lett.,* **241**(3–4), 962–971, doi:10.1016/j.epsl.2005.10.030.

Lay, T. & Wallace, T.C., 1983. Multiple ScS travel-times and attenuation beneath Mexico and Central-America, *Geophys. Res. Lett.,* **10,** 301–304.

Lay, T., Garnero, E.J. & William, Q., 2004. Partial melting in a thermo-chemical boundary layer at the base of the mantle, *Phys. Earth planet. Inter.,* **146,** 441–467.

Lee, W.S., Sato, H. & Lee, K.W., 2003. Estimation of S-wave scattering coefficient in the mantle from envelope characteristics before and after the ScS arrival, *Geophys. Res. Lett.,* **30,** doi:10.1029/2003GL018413.

Lekic, V., Matas, J., Panning, M. & Romanowicz, B., 2009. Measurement and implications of frequency dependence of attenuation, *Earth planet. Sci. Lett.,* **282,** 285–293, doi:10.1016/j.epsl.2009.03.030.

Matheney, M.P. & Nowack, R.L., 1995. Seismic attenuation values obtained from instantaneous-frequency matching and spectral ratios, *Geophys. J. Int.,* **123,** 1–15.

Minster, J.B. & Anderson, D.L., 1981. A model of dislocation-controlled rheology for the mantle, *Phil. Trans. R. Soc. Lond., A.,* **299,** 319–356.

Mégnin, C. & Romanowicz, B., 2000. The three-dimensional shear velocity structure of the mantle from the inversion of body, surface and higher-mode waveforms, *Geophys. J. Int.,* **143,** 709–728.

Müller, G., 1983. Rheological properties and velocity dispersion of a medium with power-law dependence of q on frequency, *J. Geophys.,* **54,** 20–29.

Müller, G., 1985. The reflectivity method: a tutorial, *J. Geophys.,* **58,** 153–174.

Ni, S.D. & Helmberger, D.V., 2001. Horizontal transition from fast to slow structures at the core-mantle boundary; South Atlantic, *Earth planet. Sci. Lett.,* **187,** 301–310.

Polet, J. & Kanamori, H., 2002. Anisotropy beneath California: shear wave splitting measurements using a dense broadband array, *Geophys. J. Int.,* **149,** 313–327, doi:10.1046/j.1365-246X.2002.01630.x

Resovsky, J., Trampert, J. & Van der Hilst, R.D., 2005. Error bars for the global seismic *Q* profile, *Earth planet. Sci. Lett.,* **230,** 413–423.

Rokosky, J.M., Lay, T., Garnero, E.J. & Russell, S.A., 2004. High-resolution investigation of shear wave anisotropy in D beneath the Cocos plate, *Geophys. Res. Lett.,* **31,** 1–4.

Romanowicz, B., 1995. A global tomographic model of shear attenuation in the upper mantle, *J. geophys. Res.,* **100,** 12375–12394.

Romanowicz, B., 1998. Attenuation tomography of the earth's mantle: a review of current status, *Pure appl. Geophys.,* **153,** 257–272.

Romanowicz, B. & Durek, J.J., 2000. Seismological constraints on attenuation in the earth: a review, in *Earth's Deep Interior: Mineral physics and Tomography from the Atomic to the Global Scale,* pp. 161–179, ed. Karato, S.-I., American Geophysical Union, Washington, D.C.

Romanowicz, B. & Mitchell, B., 2007. Deep Earth structure: *Q* of the Earth from crust to core. in *Treatise on Geophysics,* pp. 731–774, ed. Schubert, G., Elsevier, Frankfurt.

Saha, J.G., 1987. Relationship between Fourier and instantaneous frequency, *SEG Expanded Abstracts,* **6,** 591–594.

Schoeck, G., Shyne, J. & Bisogni, E., 1964. Activation energy of high temperature internal friction, *Acta Metall.,* **12,** 1466–1475.

Selby, N.D. & Woodhouse, J.H., 2002. The *Q* structure of the upper mantle: constraints from Rayleigh wave amplitudes, *J. geophys. Res.,* **107,** doi:10.1029/20001JB000.

Shito, A., Karato, S. & Park, J., 2004. Frequency dependence of q in earth's upper mantle inferred from continuous spectra of body waves, *Geophys. Res. Lett.,* **31,** 1–4.

Silver, P.G. & Chan, W.W., 1991. Shear wave splitting and subcontinental mantle deformation, *J. geophys. Res.,* **96,** 16 429–16 454.

Sipkin, S.A. & Jordan, T.H., 1979. Frequency-dependence of Q_{ScS}, *Bull. seism. Soc. Am.,* **69,** 1055–1079.

Tanaka, S. & Hamaguchi, H., 1992. Heterogeneity in the lower mantle beneath Africa, as revealed from S and ScS phases, *Tectonophysics,* **209,** 213–222.

Taner, M.T., Koehler, F. & Sheriff, R.E., 1979. Complex seismic trace analysis, *Geophysics,* **44,** 1041–1063.

Teng, T.L., 1968. Attenuation of body waves and *Q* structure of mantle, *J. geophys. Res.,* **73,** 2195–2205.

Thomas, C., Heesom, T. & Kendall, J.-M., 2002. Investigating the heterogeneity of the D region beneath the northern pacific using a seismic array, *J. geophys. Res.,* **107,** doi:10.1029/2000JB000021.

Thomson, D.J., 1982. Spectrum estimation and harmonic-analysis, *Proc. IEEE,* **70,** 1055–1096.

Thorne, M.S., Lay, T., Garnero, E.J., Jahnke, G. & Igel, H., 2007. Seismic imaging of the laterally varying D″ region beneath the Cocos Plate, *Geophys. J. Int.,* **170**(2), 635–648, doi:10.1111/j.1365-246X.2006.03279.x.

Tkalčić, H. & Romanowicz, B., 2002. Short scale heterogeneity in the lowermost mantle: insights from PcP-P and ScS-S data, *Earth planet. Sci. Lett.,* **201,** 57–68.

Tonn, R., 1989. Comparison of 7 methods for the computation of *Q, Phys. Earth planet. Inter.,* **55,** 259–268.

van der Baan, M., 2002. Constant *Q* and a fractal, stratified earth, *Pure appl. Geophys.,* **159,** 1707–1718.

Vidale, J.E., 1987. Waveform effects of a high velocity, subducted slab, *Geophys. Res. Lett.,* **14,** 542–545.

Wessel, P. & Smith, W.H.F., 1998. New, improved version of generic mapping tools released, *EOS, Trans. Am. geophys. Un.,* **79,** 579–579.

White, R.E., 1991. Properties of instantaneous seismic attributes, *Leading Edge,* **10,** 26–32.

White, R.E., 1992. The accuracy of estimating *Q* from seismic data, *Geophysics,* **57,** 1508–1511.

Widmer, R., Masters, G. & Gilbert, F., 1991. Spherically symmetrical attenuation within the earth from normal mode data, *Geophys. J. Int.,* **104,** 541–553.

Woodhouse, J.H. & Wong, Y.K., 1986. Amplitude, phase and path anomalies of mantle waves, *Geophys. J. R. Astr. Soc.,* **87,** 753–773.

Wysession, M.E., Fischer, K.M., Al-eqabi, G.I., Shore, P.J. & Gurari, I., 2001. Using MOMA broadband array ScS-S data to image smaller-scale structures at the base of the mantle, *Geophys. Res. Lett.,* **28,** 867–870.

Zhou, H.W. & Chen, G.M., 1995. Waveform response to the morphology of 2-D subducted slabs, *Geophys. J. Int.,* **121,** 511–522.